Ultramicroscopy 109 (2009) 929–936

Contents lists available at ScienceDirect

Ultramicroscopy

journal homepage: www.elsevier.com/locate/ultramic

Contact-resonance atomic force microscopy for nanoscale elastic property measurements: Spectroscopy and imaging

G. Stan [a,*], S. Krylyuk [b], A.V. Davydov [b], M.D. Vaudin [a], L.A. Bendersky [b], R.F. Cook [a]

[a] Ceramics Division, National Institute of Standards and Technology, 100 Bureau Drive, Gaithersburg, MD 20899, USA
[b] Metallurgy Division, National Institute of Standards and Technology, 100 Bureau Drive, Gaithersburg, MD 20899, USA

ARTICLE INFO

PACS:
62.25.−g

Keywords:
Contact-resonance atomic force microscopy
Nanoscale elastic property measurements

ABSTRACT

Quantitative measurements of the elastic modulus of nanosize systems and nanostructured materials are provided with great accuracy and precision by contact-resonance atomic force microscopy (CR-AFM). As an example of measuring the elastic modulus of nanosize entities, we used the CR-AFM technique to measure the out-of-plane indentation modulus of tellurium nanowires. A size-dependence of the indentation modulus was observed for the investigated tellurium nanowires with diameters in the range 20–150 nm. Over this diameter range, the elastic modulus of the outer layers of the tellurium nanowires experienced significant enhancement due to a pronounced surface stiffening effect. Quantitative estimations for the elastic moduli of the outer and inner parts of tellurium nanowires of reduced diameter are made with a core–shell structure model. Besides localized elastic modulus measurements, we have also developed a unique CR-AFM imaging capability to map the elastic modulus over a micrometer-scale area. We used this CR-AFM capability to construct indentation modulus maps at the junction between two adjacent facets of a tellurium microcrystal. The clear contrast observed in the elastic moduli of the two facets indicates the different surface crystallography of these facets.

1. Introduction

Mechanical property measurements at the nanoscale are critical in optimizing and predicting the performance and reliability of emerging micro- and nano-electronic and electro-mechanical devices. The metrological challenges being overcome are poised to enable reliable characterization at this scale and, in this way, provide quantification and understanding of the mechanical properties at the nanoscale: a link between atomistic simulations and micromechanical models.

Efforts dedicated to enabling non-destructive and *in situ* measurements of the elastic properties of materials at the nanoscale have produced a distinct class of atomic force microscopy (AFM)-based techniques which make use of the AFM tip-material surface dynamics: contact-resonance AFM (CR-AFM) (which includes atomic force acoustic microscopy [1] and ultrasonic AFM [2]), ultrasonic force microscopy [3], heterodyne force microscopy [4], passive overtone microscopy [5], resonant difference-frequency atomic force ultrasonic microscopy [6], and, lately, torsional harmonic dynamic force microscopy [7]. Easily implemented by adding minimal instrumentation to a commercial AFM and providing direct interpretation of the measurements, CR-AFM has been used for local point measurements as well as imaging elastic properties with nanoscale resolution. CR-AFM has been used successfully to quantify the elastic properties of a large variety of materials and structures: piezoelectric ceramics [8], metal films [9], diamond-like carbon films [10], glass-fiber-polymer matrix composites [11], clay minerals [12], polycrystalline materials [13], and nanostructures (nanobelts [14], nanowires [15], and nanotubes [16]).

In this work we demonstrate CR-AFM capabilities by providing quantitative elastic property measurements in two applications: (i) measurement of the indentation modulus of tellurium (Te) nanowires (NWs) by use of CR-AFM in spectroscopy mode and (ii) mapping of the indentation modulus of Te microcrystal facets by means of a fast CR-AFM imaging mode. In both cases, the measured contact-resonance frequencies are converted into tip–sample contact stiffness by considering the dynamics of the clamped–spring coupled cantilever and, then, by resolving the appropriate tip–sample contact geometry, the contact stiffness is converted into the local elastic modulus of the sample tested.

From CR-AFM measurements made on Te NWs of various thickness, the elastic properties of the outer surface layers of these nanostructures have been probed and surface stiffening effects observed. As the contact morphology between the spherical AFM tip and the top flat facets of Te NWs is preserved in these measurements, the change in the contact-resonance frequencies directly reflected the change in their elastic properties. A

* Corresponding author. Tel.: +1 301 975 3675; fax: +1 301 975 5995.
E-mail address: gheorghe.stan@nist.gov (G. Stan).

0304-3991/$ - see front matter © 2009 Elsevier B.V. All rights reserved.
doi:10.1016/j.ultramic.2009.03.025

consistent increase in the elastic modulus of Te NWs with a reduction in NW thickness demonstrates the size-dependence of NW surface stiffness.

Using CR-AFM imaging we have mapped the elastic modulus over micrometer-scale areas of two adjacent facets of a Te microcrystal and a different elastic contrast was observed on each facet. The facets were topographically observed to be part of some very shallow pyramidal-type structures that are formed on the otherwise flat tops of Te microcrystals. This indicates that the investigated facets could originate from nanosize-step terminations in planes of high crystallographic indices.

2. CR-AFM: spectroscopic measurements on Te nanowires

2.1. CR-AFM methodology

At small applied loads, the elastic deformation experienced by the tip–sample contact is characterized by a contact stiffness. In CR-AFM, this contact stiffness is determined from the measured resonance frequencies of the cantilever when the probe is brought into contact with the sample. These contact-resonance frequencies undergo distinct shifts from the free-resonance frequencies of the cantilever vibrated in air. The contact-resonance frequency of a given vibrational mode of the cantilever will be in the range from the free-resonance frequency of that mode to the free-resonance frequency of the next mode, depending on the mechanical properties of the material probed and the applied load. Once the contact-resonance frequencies are measured, the contact stiffness is calculated by considering the cantilever dynamics in a clamped–spring coupled beam configuration: clamped at the base of the cantilever and spring coupled at the end of the cantilever. This can be done by solving the following characteristic equation, which provides the dispersion relationship for the wavenumbers k_n^c (directly related to the contact-resonance frequencies, f_n^c) of the flexural vibrations of the clamped–spring coupled cantilever as a function of the contact stiffness $k^\star$ [1]:

$$\begin{aligned}&[\sinh k_n^c L_1 \cos k_n^c L_1 - \sin k_n^c L_1 \cosh k_n^c L_1]\\&\quad\times(1+\cos k_n^c L_2 \cosh k_n^c L_2)\\&\quad+[\cosh k_n^c L_2 \sin k_n^c L_2 - \sinh k_n^c L_2 \cos k_n^c L_2]\\&\quad\times(1-\cos k_n^c L_1 \cosh k_n^c L_1)\\&\quad=\frac{2k_c}{3k^\star}(k_n^c L_1)^3(1+\cos k_n^c L \cosh k_n^c L),\end{aligned}\tag{1}$$

where k_c is the stiffness of the cantilever. In the above equation, the tip position along the cantilever is accounted for by solving together the wave equations of flexural vibrations in the two parts delimitated by the tip along the cantilever length. The first part, of length L_1, is between the clamped base of the cantilever base the tip position. The second part, of length L_2, is between the tip position and the free end of the cantilever. The entire length of the cantilever is $L = L_1 + L_2$. For each vibrational eigenmode n of the cantilever, the wavenumbers k_n^c in the clamped–spring coupled configuration are related to the wavenumbers k_n^{free} in the clamped-free configuration by the square root of their corresponding resonance frequencies, f_n^c and f_n^{free}, respectively,

$$k_n^c = k_n^{free}\sqrt{f_n^c/f_n^{free}}.\tag{2}$$

The wavenumbers k_n^{free} can be obtained by simply solving the characteristic equation for the flexural free vibrations of the cantilever [1]:

$$1+\cos(k_n^{free}L)\cosh(k_n^{free}L)=0.\tag{3}$$

Thus, by using the solutions of Eq. (3) ($k_1^{free}L = 1.875$, $k_2^{free}L = 4.694$, ...) [1] and the measured resonance frequencies of the cantilever, in air and in contact, Eqs. (2) and (1) can be used to calculate the contact stiffness $k^\star$ normalized by the cantilever stiffness k_c. This procedure is exemplified in Figs. 1(a) and (b) for CR-AFM spectroscopic measurements on a Si(1 0 0) surface. Figs. 1(c) and (d) show how the flexural resonance vibrations of the cantilever are modified when the free end of the cantilever is attached to a spring of the same stiffness as the contact stiffness. With the measurement of at least two resonance frequencies (usually the first two modes) the position of the tip along the cantilever is also unequivocally determined from a set of two equations (1). Other factors such as lateral coupling stiffness or tilt angle of the cantilever with respect to the sample surface are ignored here as their effects are negligible for the configuration of our experiment. A complete review of the complex dynamics of the cantilever in CR-AFM can be found in Ref. [17].

The contact stiffness $k^\star$ is then related to the elastic properties of the sample through a contact model that adequately describes the established contact geometry. The loads applied in CR-AFM are greater than adhesion contact forces such that the tip–sample contact experiences repulsive contact forces in the linear elastic regime. In this case, a proper description of the contact deformation is given by the Hertz model, with the contact stiffness related to the contact radius a_c and elastic moduli of the tip and sample:

$$k^\star = 2a_c E^\star.\tag{4}$$

$E^\star = 1/(1/M_T + 1/M_S)$ is the reduced elastic modulus of the tip–sample contact and is given by a combination of the indentation moduli of the tip, M_T, and sample, M_S. In the case of an elastically isotropic material, the indentation modulus is defined simply in terms of Young's modulus E and Poisson's ratio ν, $M = E/(1-\nu^2)$. Anisotropic contributions to the indentation modulus can be addressed either theoretically [27] or experimentally [13].

The necessity for knowing the contact radius in Eq. (4) is obviated by making successive CR-AFM measurements on the sample tested and a reference material with known elastic

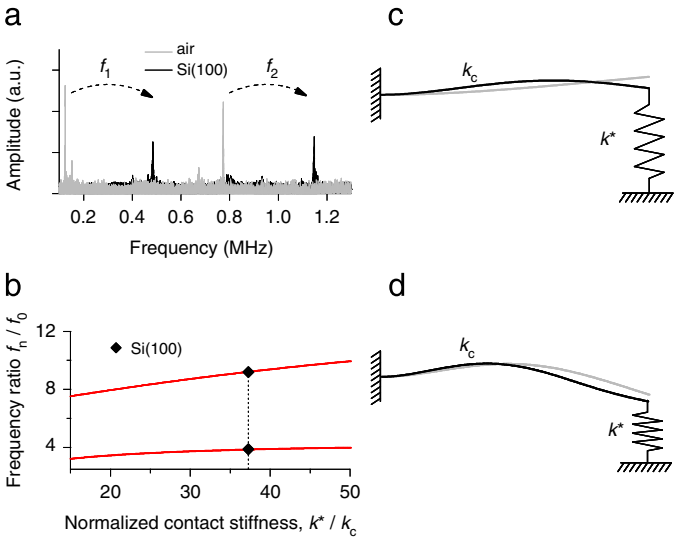

Fig. 1. (a) The shifts in the first and second resonance frequencies of a cantilever from air to contact on Si(1 0 0). (b) With the resonance frequencies shown in (a), the contact stiffness between tip and Si(1 0 0) is calculated by using the clamped–spring coupled model for the cantilever [1] (continuous curves). First (c) and second (d) flexural resonance vibrations of the free and spring-coupled cantilever with the contact stiffness calculated in (b).

modulus. By taking the ratio of the measured contact stiffnesses on the sample, $k_S^\star$, and reference, $k_R^\star$, the elastic modulus of the sample, M_S, is calibrated with respect to that of the reference, M_R, by

$$1/M_S = (k_R^\star/k_S^\star)^n/M_R + [(k_R^\star/k_S^\star)^n - 1]/M_T, \quad (5)$$

where $n = 1$ for a flat tip and $n = \frac{3}{2}$ for a spherical tip in contact with a flat surface. Furthermore, the use of two reference materials eliminates the need for knowing or assuming a value for the indentation modulus of the tip [28].

2.2. Experimental set-up for CR-AFM spectroscopy

In CR-AFM, to measure the contact-resonance frequencies of the system, the contact is mechanically vibrated by a very small amplitude oscillation at frequencies in the kilohertz to megahertz range. In our experimental set-up, a lock-in amplifier with internal signal generator (7280 Signal Recovery AMETEK, Oak Ridge, TN, USA) [29] was used to vibrate the cantilever of the probe brought in contact with the sample (in this work the top facets of Te NWs). In each CR-AFM measurement, the modulation frequency was swept over large ranges to detect the shift in the cantilever resonances. The contact-resonance frequencies were identified in the high-frequency response collected from the AFM photodiode detector. The instrumentation needed in these CR-AFM measurements was developed on a LabView (National Instruments, Austin, TX, USA) [29] base and attached to a commercial AFM (Veeco MultiMode II, Santa Barbara, CA, USA) [29]. The AFM probes (PPP-SEIH NanoSensors, Neuchatel, Switzerland) [29] used in this work were single-crystal Si cantilevers made with integrated Si[1 0 0] tips. The spring constant of the cantilevers used was around 10 N m^{-1} as determined from measurements of their thermal-noise [26]. A constant static load, about 250 nN, was applied to the tip–sample contact in each measurement. This load was large enough to exceed the adhesion forces but small enough to maintain the contact deformation in the elastic regime and produce no contribution from the Si substrate for Te NWs thicker than 20 nm.

2.3. Te NWs fabrication and structure analysis

In the past few years, the synthesis of Te nanostructures in form of nanowires, nanobelts, and nanotubes has received distinct attention [18–22]. Such efforts are aiming to exploit various conducting, photoconducting, thermoelectric, and piezoelectric properties of Te in developing new nanoscale electronic and optoelectronic devices [23–25].

In this work, Te nanostructures were fabricated on Si(1 0 0) substrates by a vapor-transport deposition method. A quartz boat with high purity elemental Te powder (99.99%, Alfa Aesar, Ward Hill, MA, USA) was placed in the central part of a horizontal alumina tube furnace. Several Si(1 0 0) substrates, ultrasonically cleaned in acetone and isopropanol, were placed downstream at different locations; the temperature of these locations was determined prior to the growth by measuring the temperature profile of the furnace. Before deposition, the system was evacuated to about 60 Pa and purged with ultra-high purity gas (5% $H_2 - N_2$). The furnace was heated to 450 °C (the melting temperature of Te), kept at this temperature for 120 min, and then slowly cooled with continuous gas flow of 100 sccm. Although Te nanostructures in the form of wires, rods, and branched structures were obtained for any condensation temperature in the range 130–250 °C, deposition at the selected temperature of 180 °C mainly produced straight NWs (2–10 μm long) of uniform cross-section (see Figs. 2(a) and (b)). Under such conditions, Te NWs have been observed to grow parallel to the substrate, both ends exhibiting the same morphology.

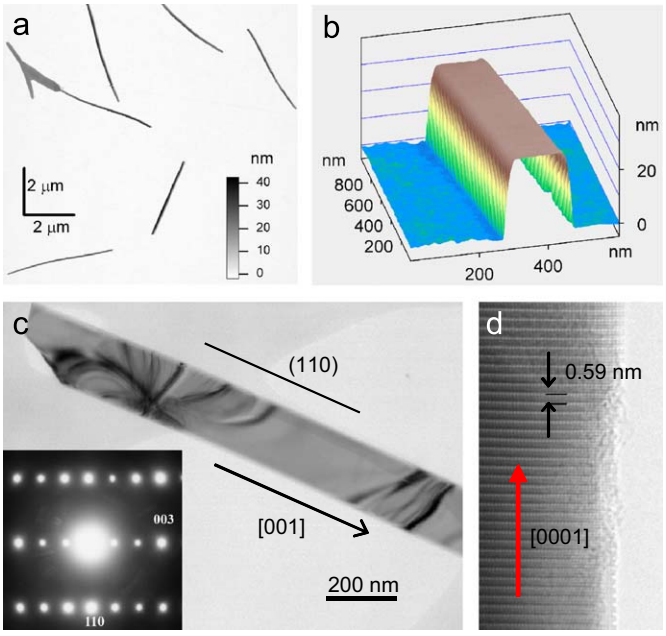

Fig. 2. AFM images (a) encompassing many Te NWs dispersed on a Si substrate as well as (b) a selected region of a single Te NW show the uniform cross-section and flatness of the top facets of these NWs. (c) Based on the observed diffraction pattern (insert), the crystallographic orientation of one of the Te NWs is shown on the TEM image. (d) Portion of the NW shown in (c) is further detailed by high-resolution TEM.

Energy-dispersive X-ray spectroscopy studies confirmed that the grown nanostructures consist of Te and X-ray diffraction spectra were indexed to pure hexagonal Te. The crystallographic structure of Te NWs measured in this work was further elucidated by transmission electron microscopy (TEM). As is shown in Figs. 2(c) and (d), the single-crystal structure and orientation along [0 0 0 1] direction of Te NWs were revealed in such investigation from diffraction patterns as well as high-resolution TEM images. In addition, the morphology and structure of Te NWs were also investigated using a field emission scanning electron microscope (FESEM) (Hitachi S-4700-II, Hitachi Ltd., Tokyo, Japan) equipped with an electron backscatter diffraction (EBSD) detector. EBSD patterns on the top facets of Te NWs (see Fig. 3) matched simulated patterns for the Te structure and showed that the NWs growth direction was the *c*-axis; all the investigated top facets were found to be in the same $\{1\,0\,\bar{1}\,0\}$ plane of the Te hexagonal lattice.

2.4. CR-AFM measurements on Te NWs

CR-AFM measurements were performed on Te NWs with thicknesses in the 20–150 nm range. Each NW probed by CR-AFM was first located on the substrate by intermittent-contact mode AFM. A high-resolution topographical image (as in Fig. 2(b)) was acquired to determine accurately the NW thickness from the height difference between the top facet of the NW and the plane of the substrate. Then, a set of at least five CR-AFM measurements were made back and forth on top of the NW and the substrate. The average values of the first and second contact-resonance frequencies on each probed Te NW and the Si(1 0 0) substrate were used to calculate the contact stiffnesses by means of Eq. (1). Their ratio, $k_{NW}^\star/k_{Si(1\,0\,0)}^\star$, was then converted into the indentation modulus of the NW using Eq. (5). Thus, the uncertainty in the elastic modulus values is determined by the measurement uncertainties in the

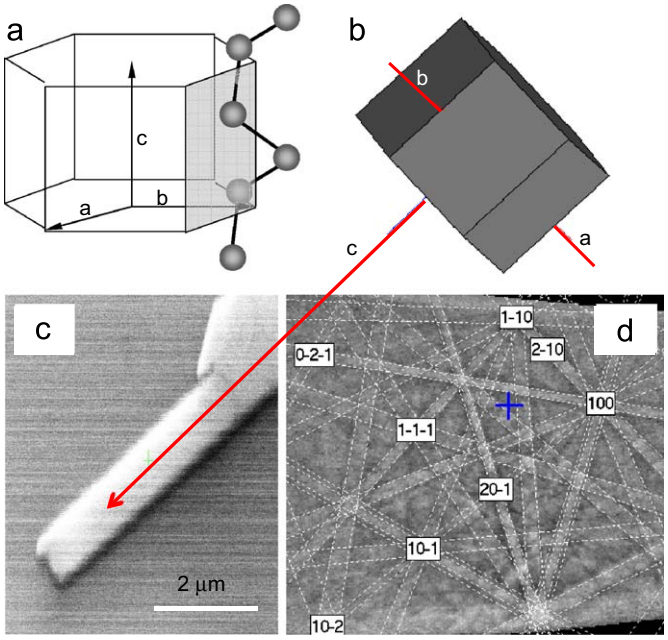

Fig. 3. (a) The crystallographic structure of Te is generated by attaching to each node of its hexagonal lattice three atoms along helical chains that are parallel to the *c*-axis ([0 0 0 1] direction). (b) and (c) The orientation of the Te hexagonal cell found from EBSD analysis made on the top facet of a NW. (d) EBSD pattern on the top facet of the Te NW shown in (c).

contact-resonance frequencies. A possible reason for the observed variations in the measured contact-resonance frequencies could be in the small variations that occur in the contact area at every different contact point, either due to the surface roughness, slight variations in the applied load, or local variations in the elastic properties of the specimen tested. In the following, the uncertainty in the elastic modulus values represents one standard deviation in the observed experimental values. The indentation moduli of the reference substrate and the tip were assumed to be $M_{\mathrm{Si}(1\,0\,0)} = 164.8\,\mathrm{GPa}$, calculated as in Ref. [26] for a Si(1 0 0) surface normally indented by a round tip.

With an applied load of about 250 nN, the first and second contact resonances on Te NWs and Si(1 0 0) substrate were found to vary in the 400–600 and 1000–1200 kHz ranges, respectively. As an example, in Fig. 4 are shown the shifts in the first and second resonance frequencies from air to contact for a measured NW (76 nm thick) and the Si(1 0 0) substrate. The difference between the resonance frequencies measured on Si(1 0 0) and Te NWs was observed to decrease as Te NWs of thickness less than 100 nm were probed. This size-dependence in the elastic response of Te NWs was quantified as indentation modulus and is shown in Fig. 5(a) as a function of NWs thickness. We can see in Fig. 5(a), that the indentation modulus is constant, around 45 GPa, for NWs thicker than 100 nm, monotonically increases from 45 to 85 GPa for NWs with thickness in the 100–30 nm range, and plateaus around 85 GPa for NWs thinner than 30 nm. This size-dependence of NWs elastic modulus differs from that previously reported for other types of NWs: over the investigated diameter range, a continuous increase in the elastic modulus was found with the reduction in diameter [30–33,15] but no plateau was observed in the range of very small diameters.

The size-dependence observed in the elastic response of NWs of reduced diameters [30–34,15] originates from the surface energy and surface stress effects in such nanostructures with large surface-to-volume ratio [35–39]. Symmetry destruction as well as relaxation of bonds due to uncoordinated atoms in the surface layers of NWs modify the surface energy, which, in turn, affects

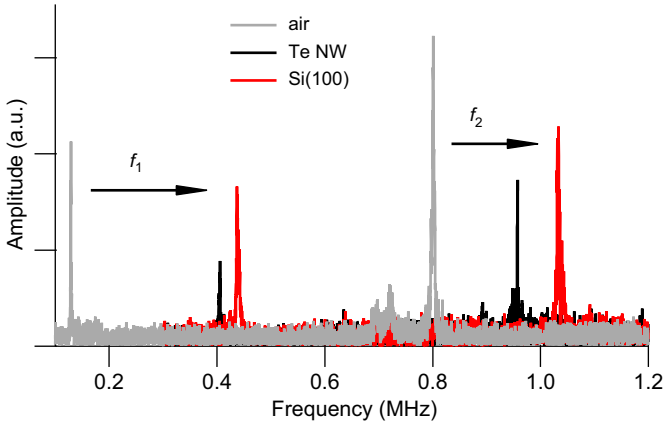

Fig. 4. Shifts in the resonance frequencies of the cantilever from air to contact on Si(1 0 0) and Te NW of thickness 76 nm.

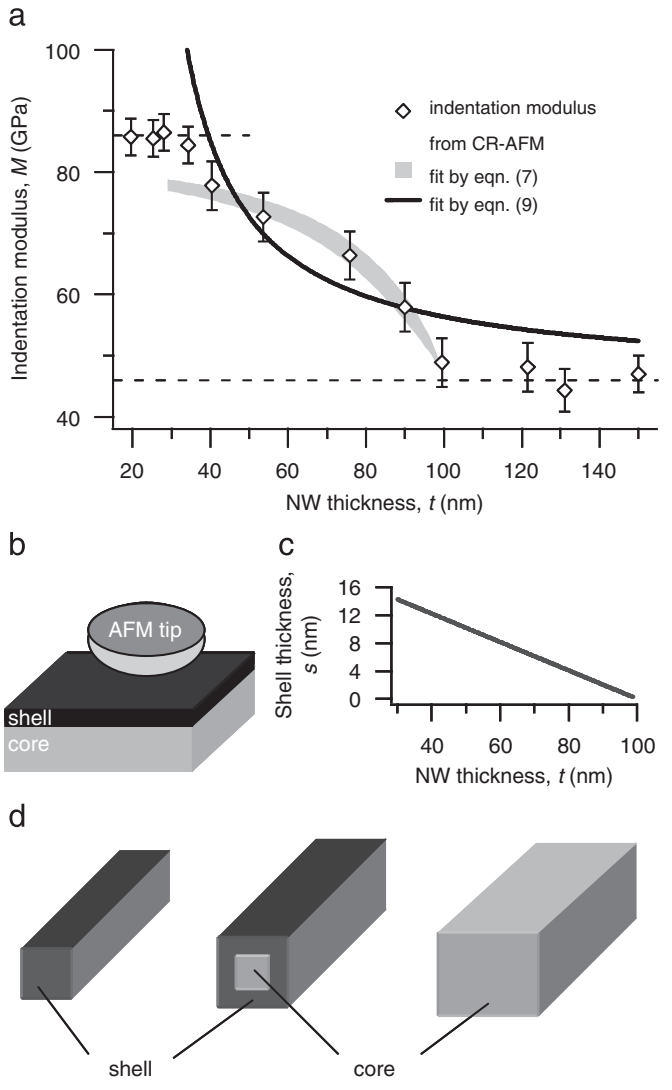

Fig. 5. (a) Indentation modulus of Te NWs as a function of thickness: experimental measurements (diamond symbols) and fitting curves (the gray band is provided by Eq. (7) and black curve by Eq. (9); see text for details). The dotted lines represent the observed limits of the indentation modulus of very thin and very thick Te NWs, respectively. (b) Spherical tip indenting a core–shell structure (as in the case of a coated substrate) (c) a linear shell thickness versus NW thickness was assumed over the variable modulus range. (d) Schematic diagram of the core–shell structure from very thick NWs (mostly core) to very thin NWs (mostly shell).

the mechanical properties of NWs. The measured elastic modulus deviates from the bulk value due to the morphological changes that progressively occur in the outer layers as the NW cross-section shrinks. Thus, to accommodate the stress, the lattice in the outer layers undergoes contraction and places the inner material into compression. As a result, the surface stiffness is enhanced and revealed, for example, in measurements of apparent elastic modulus of nanowires of reduced cross-section.

A simple way to distinguish the surface stiffness contribution to the measured elastic modulus of NWs is to consider the NW as made of a core with the same elastic properties as the bulk material and a stiffer shell, coaxial with the core [32]. To accommodate the observed plateaus in the measured elastic modulus of Te NWs, we assume here a linear variation of the shell thickness as a function of the NW thickness over the elastic modulus size-dependent range [34]; to a first approximation, this is also consistent with a progressive lattice relaxation in the outer layers. Thus, for NWs thicker than a threshold thickness, t_{max}, the elastic response is mainly determined by the core, the shell being of negligible thickness. As the NW thickness is reduced below t_{max}, the shell, made of stiffer layers, become thicker and contributes more to the apparent elastic modulus. The core diminishes to zero at a critical NW thickness, t_{min}, below which the measured elastic modulus is that of the shell. With these considerations, a linear dependence of the shell thickness s on the NW thickness t is given by

$$s = \frac{t_{min}(t_{max} - t)}{2(t_{max} - t_{min})}. \quad (6)$$

We can separate the elastic contributions of the core and shell to the measured elastic modulus by considering the case of the round tip indenting the composite core–shell structure as in the case of a coated substrate. In our case, the substrate is substituted by the core and the film by the shell (see Fig. 5(b)). Because the contact radius is negligible compared to the width of NWs, even for the thinnest NW, the indented top NW facet is basically an infinite surface and no edge corrections are needed. An analytical solution for the indentation modulus of such a layered system is provided by Gao's model [40]:

$$M = I(\xi)M_{shell} + [1 - I(\xi)]M_{core}, \quad (7)$$

where M_{core} and M_{shell} are the indentation moduli of the core and shell, respectively. The dependence of the indentation modulus M on the shell thickness s and the contact radius a is given by the parameter $\xi = s/a$ in the weighting function I:

$$I(\xi) = \frac{2}{\pi}\arctan(\xi) + \frac{[(1-2\nu)\xi(1+\xi^{-2}) - \xi/(1+\xi^2)]}{2\pi(1-\nu)}. \quad (8)$$

Poisson's ratio ν is considered to be constant through the entire layered structure.

We have applied Gao's model to fit the indentation modulus of Te NWs over the range where presumably the shell varies in thickness, between the two plateaus. We interpret the meaning of these plateaus as following. In the limit case of very thick NWs, the shell part is negligible, so the measured modulus is constant and corresponds to the bulk value. In the limit of very thin NWs (thinner than 30 nm for Te NWs), the stiff outerlayers make up almost the entire thickness, and the measured modulus is that of the shell. Thus, from these plateaus, we extract $M_{core} = 46$ GPa and $M_{shell} = 85$ GPa. With these values, a good fit is given by Gao's model in the transition region with the fit parameters $t_{max} = 100$ nm, $t_{min} = 29$ nm, and $a = 4.0$ nm. The fit is shown in Fig. 5(a) within the gray band as Poisson's ratio was varied from 0.1 (upper edge) to 0.4 (lower edge). In Fig. 5(c) is shown the linear dependence of the shell thickness s as a function of the NW thickness t over the fitting range. The model ceases to be applicable in the range of very thin NWs (i.e., below 30 nm) where the core thickness diminishes so much that is not a substrate anymore for the indented shell. The fit parameter $a = 4.0$ nm agrees well with the contact radius $a_{Hertz} = 4.2$ nm calculated with the Hertz model, $a_{Hertz} = (3PR_T/4E^\star)^{1/3}$, for a load $P = 250$ nN, a reduced elastic modulus $E^\star = 50$ GPa, and a tip radius $R_T = 20$ nm. As the sensing depth of CR-AFM is about three times the contact radius [41], the substrate contribution to our measurements is negligible for all the NWs probed.

A schematic diagram of the core–shell partition of the NW cross-section is shown in Fig. 5(d) as a function of the NW thickness. In the range of very thin NW, where presumably the shell extends over the entire NW, the indentation modulus is almost constant suggesting that the attendant lattice contraction and disorder are now less of an energy penalty than that required to adjust to the equilibrium interatomic spacing of the bulk core. The average shell thickness of the Te NWs measured in this work, $t_{min}/4 = 7.2$ nm, is in the range of shell thicknesses calculated for ZnO NWs, 4.4 [32] and 12 nm [15], respectively.

A less accurate fit is obtained if a shell of constant thickness [32] is considered over the size-dependent elastic modulus region. Thus, with s_{avrg} constant for the shell thickness, the indentation modulus of the core–shell structure is simply estimated by considering a uniform stress distribution in the cross-section of the NW of variable thickness t, which gives [15]

$$\frac{t}{M} = \frac{s_{avrg}}{M_{shell}} + \frac{t - s_{avrg}}{M_{core}}. \quad (9)$$

The fit given by Eq. (9) is shown by the thick black curve in Fig. 5(a). Excepting the region of very thin NWs, the fit works reasonably well with the following parameters: $M_{core} = 46$ GPa, $M_{shell} = 85$ GPa, and $s_{avrg} = 20$ nm. As we can see, the dependence given by Eq. (9) predicts a continuous increase in the elastic modulus as the NW cross-section is reduced, and no plateau is obtained for the measurements made on Te NWs thinner than 30 nm.

To conclude this section, by using CR-AFM we measured the elastic modulus of Te NWs with thickness in the 20–150 nm range. The observed size-dependent indentation modulus in the 30–100 nm thickness range is well explained by the assumed linear core–shell partition of NW cross-section. The intrinsic indentation modulus of the shell, directly probed for NWs thinner than 30 nm, is about twice that of the bulk core (measured on very thick NWs). This enhancement factor is similar to that calculated for the size-dependent elastic modulus of Ag and Pb metallic NWs [30,31], although no evidence for an elastic modulus saturation was observed in those measurements as the NW diameter was reduced.

3. CR-AFM: imaging the elastic modulus of Te microcrystal facets

3.1. Instrumentation development for CR-AFM imaging

CR-AFM imaging was accomplished by performing CR-AFM spectroscopic measurements at each point in an image scan [42]. Additional instrumentation developed in LabView was used to coordinate the sequence of operations required in this scheme (see Fig. 6): while the AFM feedback was maintained active, so the tip followed the topography, the in-plane displacement of the tip was externally controlled by applying incremental voltages on x- and y-piezo scanners (sequence 1). Then, at each point in the scan, the cantilever was mechanically vibrated by a sinusoidal oscillation (sequences 2 and 3), in the same way as in point-based CR-AFM spectroscopy. The frequency of the signal was swept over the range where presumably the contact resonance would be found.

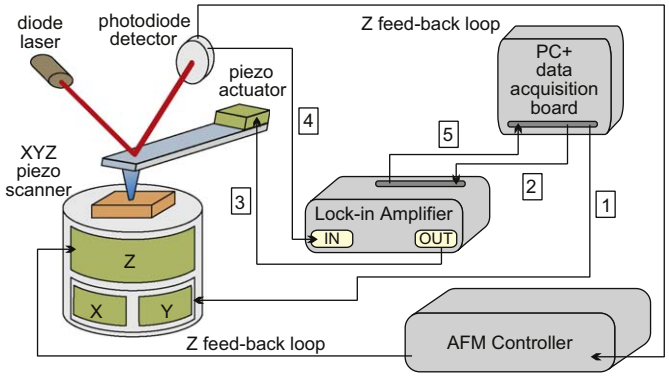

Fig. 6. Additional instrumentation needed for CR-AFM was attached to a commercial AFM. The numbers indicate the sequence of events made at every point in an image scan.

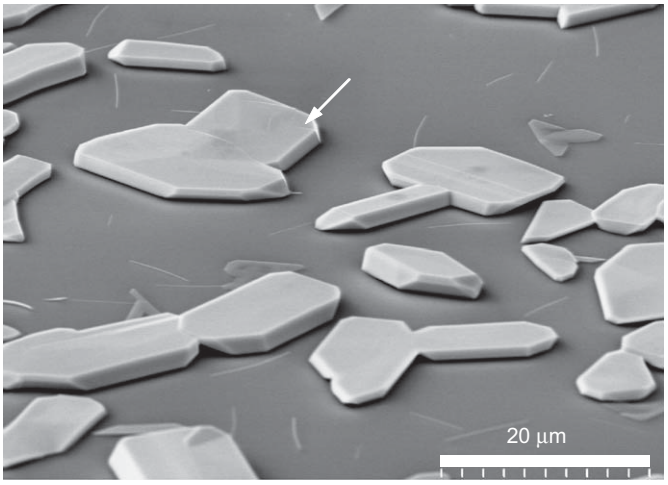

Fig. 7. Tilted SEM image of Te microcrystals grown on a Si(1 0 0) substrate. Te microcrystals are in form of flat prisms, a few μm tall and basal areas of tens to hundreds of μm square. Sparse nanowires are also observed around these microcrystals.

At the same time (sequences 4 and 5), the high-frequency response was collected from the AFM photodiode through a lock-in amplifier detection. On one hand, a reduced frequency range increases acquisition speed, but, on the other hand, the range needs to be large enough to encompass the contact-resonance frequency shifts. During scanning, visualization of frequency spectra allows inspection, to see if the resonance peak is still in the chosen range or not. After scanning, by analyzing the recorded frequency spectra, the resonance frequency is identified at each point in the scan and the contact-resonance map generated.

3.2. Te microcrystals fabrication and morphology characterization

Besides Te NWs, we also investigated the elastic properties of some Te microcrystals, which are in form of flattened prisms with irregular polygonal bases (see Fig. 7). Te microcrystals were grown in the same run as Te NWs described in the previous section. The larger size of the microcrystals compared to those of NWs was determined by the different temperature at which they were deposited. The microcrystals were grown on Si substrates kept at 220 °C (i.e., closer to the boat with Te powder). Occasionally, on the same sample with microcrystals some thick nanowires or nanobelts were also observed. As can be seen in Fig. 7, these prismatic Te microcrystals are few μm thick, have large geometrical aspect ratios (width to thickness and length to thickness ratios), and their basal planes are essentially flat at the micrometer scale. However, if we used AFM imaging to look at the nanoscale, inverse pyramidal structures (inverse hillocks) are observed on these otherwise flat top facets of the microcrystals (see Figs. 8(a)–(d)). The origin of inverse hillocks can be associated with the anisotropic growth rates of Te rather than structural defects. It is conceivable that, during vapor deposition, the out-of-plane growth slightly dominates the in-plane migration and growth, and this determines incomplete layer formations in form of shallow depressions (inverse hillocks). From EBSD patterns made on the flat part of the top facets of various Te microcrystals, we identified the prismatic bases of these microcrystals as being in the same $\{1\,0\,\bar{1}\,0\}$ plane of the Te hexagonal lattice. We used CR-AFM imaging to map the elastic modulus at the joint of two such pyramidal facets. The AFM images shown in Figs. 8(a)–(d) were processed by using the WSxM 4.0 software package [43].

3.3. Elastic modulus map reconstruction on two adjacent facets of a Te microcrystal

From the frequency spectra recorded during CR-AFM imaging, the first contact-resonance frequency was identified at every point in the scan and used to generate, pixel by pixel, the image shown in Fig. 8(e). A different contrast is observed between these two facets in the contact-resonance frequency map: the average value is 458.7 ± 2.1 kHz on the left side and 456.2 ± 2.6 kHz on the right side. The magnitude of this contrast difference cannot be explained by the change in the tilt of the cantilever on each facet, this angular change being too small to have a noticeable contribution to the contact stiffness. Moreover, the tilt contribution to the contact-resonance frequency map was ruled out also by observing that the contrast is preserved along the multi-atomic steps and differed only over the flat parts. Consequently, we can attribute the observed contrast in the mapped contact-resonance frequency to a difference in the mechanical properties of the two inspected facets.

The average contact-resonance frequencies obtained from CR-AFM imaging on the two pyramidal facets were used to calculate the contact stiffnesses characterizing the contact made by the tip on these facets. These contact stiffnesses are shown in Fig. 9 together with those calculated from individual CR-AFM measurements (at least five) on the flat region (lower right part in Figs. 8 (a) and (b)) of the Te microcrystal top and on the Si(1 0 0) substrate. It can be seen that each of the mapped facets of the inverted pyramid appears stiffer than the flat top of the prismatic microcrystal. Using the Si(1 0 0) as a reference material, the contact stiffnesses measured on the Te facets were converted into indentation moduli with the help of Eq. (5). The value of the indentation modulus on the flat region of the top, $M_{\text{Te, flat top}} = 46.1 \pm 2.9$ GPa is in excellent agreement with that measured on Te NWs thicker than 100 nm. Regarding the two pyramidal facets, it turned out that their indentation moduli differed only marginally from each other: $M_{\text{Te, left facet}} = 54.8 \pm 2.5$ GPa and $M_{\text{Te, right facet}} = 51.9 \pm 2.7$ GPa. This indicates that the two facets, resulting from nanosize-step terminations, are in planes of high crystallographic indices, at small angular orientations with respect to the $(1\,0\,\bar{1}\,0)$ plane of Te lattice.

The small difference measured between the elastic modulus of the two pyramidal facets of the Te microscrystal demonstrates the sensitivity of CR-AFM imaging in providing quantitative measurements of the elastic properties over μm-size area. Nanoscale variations of the elastic modulus can be identified in such images and correlated with the topography of the scanned surface.

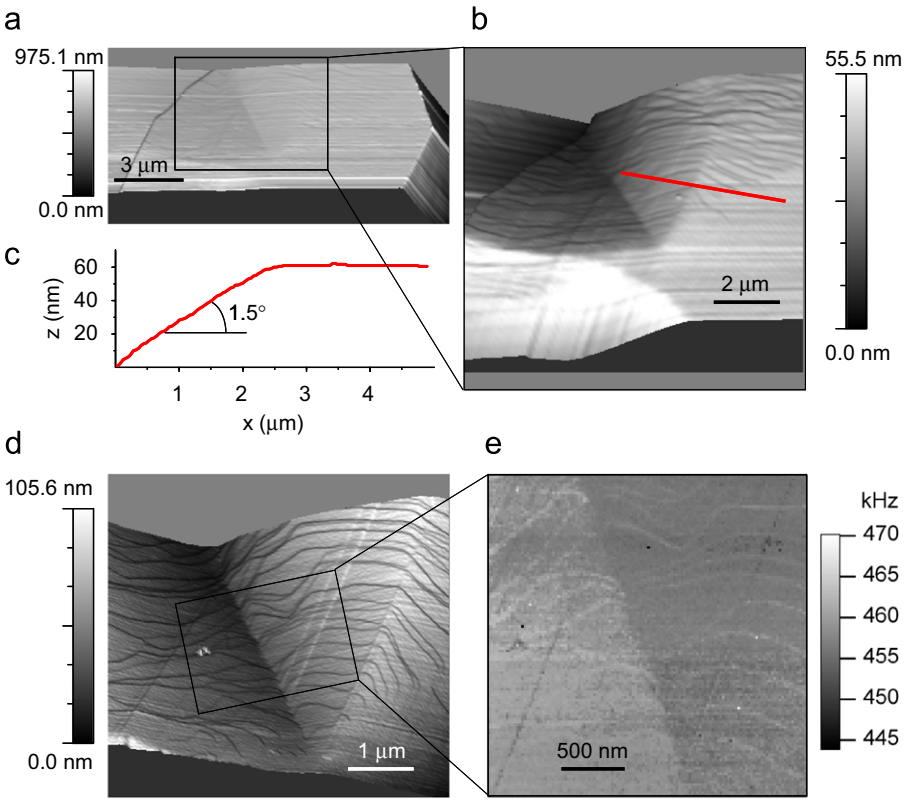

Fig. 8. AFM topographies (a–d) and CR-AFM map (d) over selected areas of a Te microcrystal: (a) The region indicated by an arrow in Fig. 7 was detailed by AFM. (b) The rectangular window shown in (a) is further detailed and the wedge angles of the pyramidal depression are observed with respect to the flat part. (c) Topographical profile along the line shown in (b) is used to calculate the wedge angle formed by the pyramidal facet with the flat top facet of the microcrystal. (d) The joint between the two pyramidal facets is shown in detail; atomic plane terminations are observed in this AFM topographical image. (e) The first contact-resonance frequency was mapped over the selected window shown in (d) by CR-AFM imaging.

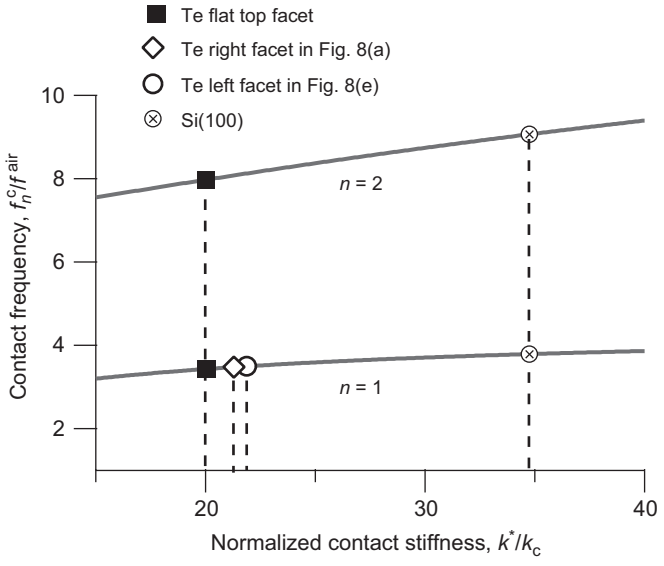

Fig. 9. Contact frequency (normalized to the first free resonance frequency of the cantilever) versus contact stiffness (normalized to the cantilever stiffness). The continuous curves are calculated by using the clamped–spring coupled cantilever model [1]. The data points are from CR-AFM imaging shown in Fig. 8(e) and from point-based measurements on the flat top of a Te microcrystal and Si(1 0 0) surface, respectively.

4. Conclusions

CR-AFM spectroscopy and imaging modes were used to quantitatively measure the elastic modulus of Te NWs and microcrystals. A size-dependence was observed in the indentation modulus of Te NWs with thicknesses in the 20–150 nm range. Stiffening effects were revealed in the elastic modulus of Te NWs thinner than 100 nm, whereas the indentation modulus of Te NWs thicker than 100 nm was found to be the same as on flat facets of Te microcrystals. A distinct contrast in the elastic properties was probed by CR-AFM imaging on two Te microcrystal facets of slightly different orientation.

References

[1] U. Rabe, K. Janser, W. Arnorld, Rev. Sci. Instrum. 67 (1996) 3281.
[2] K. Yamanaka, S. Nakano, Jpn. J. Appl. Phys. 35 (1996) 3787.
[3] O. Kolosov, K. Yamanaka, Jpn. J. Appl. Phys. 32 (1993) L1095.
[4] M.T. Cuberes, H.E. Assender, G.A.D. Briggs, O.V. Kolosov, J. Phys. D Appl. Phys. 33 (2000) 2347.
[5] T. Drobek, R.W. Stark, W.M. Heckl, Phys. Rev. B 64 (2001) 045401.
[6] S.A. Cantrell, J.H. Cantrell, P.T. Lillehei, J. Appl. Phys. 101 (2007) 114324.
[7] O. Sahin, S. Magonov, C. Su, C.F. Quate, O. Solgaard, Nat. Nanotech. 2 (2007) 507.
[8] U. Rabe, M. Kopycinska, S. Hirsekorn, J. Munoz Saldana, G.A. Schneider, W. Arnold, J. Phys. D Appl. Phys. 35 (2002) 2621.
[9] M. Kopycinska-Muller, R.H. Geiss, J. Muller, D.C. Hurley, Nanotechnology 16 (2005) 703.

[10] D. Passeri, A. Bettucci, M. Germano, M. Rossi, A. Alippi, Appl. Phys. Lett. 88 (2006) 121910.
[11] D.C. Hurley, M. Kopycinska-Muller, A.B. Kos, R.H. Geiss, Adv. Eng. Mater. 7 (2005) 713.
[12] M. Prasad, M. Kopycinska, U. Rabe, W. Arnold, Geophys. Res. Lett. 29 (2002) 31.
[13] A. Kumar, U. Rabe, S. Hirsekorn, W. Arnold, Appl. Phys. Lett. 92 (2008) 183106.
[14] Y.G. Zheng, R.E. Geer, K. Dovidenko, M. Kopycinska-Muller, D.C. Hurley, J. Appl. Phys. 100 (2006) 124308.
[15] G. Stan, C.V. Ciobanu, P.M. Parthangal, R.F. Cook, Nano Lett. 7 (2007) 3691.
[16] G. Stan, C.V. Ciobanu, T.P. Thayer, G.T. Wang, J.R. Creighton, K.P. Purushotham, L.A. Bendersky, R.F. Cook, Nanotechnology 20 (2009) 035706.
[17] U. Rabe, in: B. Bushan, H. Fuchs (Eds.), Applied Scanning Probe Methods II, Springer, Berlin, 2006, pp. 37–90.
[18] B. Mayers, Y. Xia, J. Mater. Chem. 12 (2002) 1875.
[19] Y. Xia, P. Yang, Y. Sun, Y. Wu, B. Mayers, B. Gates, Y. Yin, F. Kim, Y. Yan, Adv. Mater. (Weiheim Ger.) 15 (2003) 353.
[20] Q. Lu, F. Gao, S. Komarneni, Adv. Mater. 16 (2004) 1629.
[21] U.K. Gautam, C.N.R. Rao, J. Mater. Chem. 14 (2004) 2530.
[22] X.-L. Li, G.-H. Cao, C.-M. Feng, Y.-D. Li, J. Mater. Chem. 14 (2004) 244.
[23] A.A. Kudryavstev, The Chemistry and Technology of Selenium and Tellurium, Collet's Ltd., London, 1974.
[24] P. Tangney, S. Fahy, Phys. Rev. B 65 (2002) 054302.
[25] Y. Wang, Z. Tang, P. Podsiadlo, Y. Elkasabi, J. Lahann, N.A. Kotov, Adv. Mater. 18 (2006) 518.
[26] J.L. Huttler, J. Bechhoefer, Rev. Sci. Instrum. 64 (1993) 1868.
[27] J.J. Vlassak, W.D. Nix, Philos. Mag. A 67 (1993) 1045.
[28] G. Stan, W. Price, Rev. Sci. Instrum. 77 (2006) 103707.
[29] Any mention of commercial products in this article is for information only; it does not imply recommendation or endorsement by the National Institute of Standards and Technology.
[30] S. Cuenot, C. Fretigny, S. Demoustier-Champagne, B. Nysten, Phys. Rev. B 69 (2004) 165410.
[31] G.Y. Jing, H.L. Duan, X.M. Sun, Z.S. Zhang, J. Xu, Y.D. Li, J.X. Wang, D.P. Yu, Phys. Rev. B 73 (2006) 235409.
[32] C.Q. Chen, Y. Shi, Y.S. Zhang, J. Zhu, Y.J. Yan, Phys. Rev. Lett. 96 (2006) 075505.
[33] E.P.S. Tan, Y. Zhu, T. Yu, L. Dai, C.H. Sow, V.B.C. Tan, C.T. Lim, Appl. Phys. Lett. 90 (2007) 163112.
[34] G. Stan, S. Krylyuk, A.V. Davydov, M. Vaudin, L.A. Bendersky, R.F. Cook, Appl. Phys. Lett. 92 (2008) 241908.
[35] R.E. Miller, V.B. Shenoy, Nanotechnology 11 (2000) 139.
[36] A.J. Kulkarni, M. Zhou, F.J. Ke, Nanotechnology 16 (2005) 2749.
[37] Y. Wen, Y. Zhang, Z. Zhu, Phys. Rev. B 76 (2007) 125423.
[38] J. He, C.M. Lilley, Nano Lett. 8 (2008) 1798.
[39] C.Q. Sun, B.K. Tay, X.T. Zeng, S. Li, T.P. Chen, J. Zhou, H.L. Bai, E.Y. Jiang, J. Phys. Condens. Matter 14 (2002) 7781.
[40] H. Gao, C.-H. Chiu, J. Lee, Int. J. Solids Struct. 29 (1992) 2471.
[41] U. Rabe, S. Amelio, M. Kopycinska, S. Hirsekorn, M. Kempf, M. Goken, W. Arnold, Surf. Interface Anal. 33 (2002) 65.
[42] G. Stan, R.F. Cook, Nanotechnology 19 (2008) 235701.
[43] I. Horcas, R. Fernandez, J.M. Gomez-Rodriguez, J. Colchero, J. Gomez-Herrero, A.M. Baro, Rev. Sci. Instrum. 78 (2007) 013705.